Article

Effect of Laser Surface Texturing on Schmid Factor and Plastic Deformation Mechanisms on AISI 301LN Steel

Mohammad Rezayat, Joan Josep Roa and Antonio Mateo

Article

Effect of Laser Surface Texturing on Schmid Factor and Plastic Deformation Mechanisms on AISI 301LN Steel

Mohammad Rezayat [1,2,*] , **Joan Josep Roa** [1,2] and **Antonio Mateo** [1,2]

1 Center for Structural Integrity, Micromechanics, and Reliability of Materials (CIEFMA), Department of Materials Science and Engineering, Universitat Politècnica de Catalunya-BarcelonaTECH, 08019 Barcelona, Spain; jj.roa@gpainnova.com (J.J.R.); antonio.manuel.mateo@upc.edu (A.M.)
2 Barcelona Research Center in Multiscale Science and Engineering, Universitat Politècnica de Catalunya-BarcelonaTECH, 08019 Barcelona, Spain
* Correspondence: mohammad.rezayat@upc.edu

Abstract: In this comprehensive study, the multifaceted impact of laser surface texturing (LST) on AISI 301LN stainless steel is explored. Changes in the microstructure, mechanical properties, and grain characteristics are examined. The dynamic relationship between Schmid factor evolution and plastic deformation in this stainless steel alloy is unveiled through the analysis of grain statistics and individual grain scrutiny. It is revealed that LST initiates the formation of strain-induced α'-martensite, grain refinement, and substantial hardness enhancements. Notably, an α'-martensite crystalline size of 2.05 Å is induced by LST. Furthermore, a 12% increase in tensile strength is observed after LST along with an 11% boost in yield strength. However, reductions of 19% in elongation to fracture and 12% in the area reduction are experienced.

Keywords: Schmid factor; laser surface texturing; metastable stainless steel; TRIP; deformation mechanisms

1. Introduction

In the relentless pursuit of improving the mechanical properties of structural materials, particularly in the automotive industry, the focus has shifted towards high-strength steels [1,2]. Indeed, high-strength steels encompass a diverse range of materials, each distinguished by its unique microstructural and mechanical characteristics. One prominent class of these advanced materials is renowned for its exceptional strength, achieved through the development of robust solid-state transformation products, most notably due to the martensitic phase (α'- and/or ε-). This phase is intricately embedded within a relatively softer austenitic (γ-) matrix, forming a distinctive microstructural blend [3–5]. It is important to emphasize that the high-strength steel landscape encompasses various microstructures beyond the martensite–austenite combination, making it a rich and multifaceted domain. This diversity not only contributes to their remarkable strength but also confers these materials' noteworthy ductility [6,7]. The martensitic phase transformation, characterized by a rapid and diffusionless nature, has captivated researchers for over a century and continues as a subject of profound interest and investigation [8–11].

The conceptual foundation for transformation-induced plasticity (TRIP) steels, which utilize martensitic phase transformations to enhance ductility, was laid by Zackay et al. [12]. TRIP steels owe their high strength and improved ductility to a composite-like structure, wherein the hard martensitic phase resides within the soft austenitic matrix, akin to a composite material reinforced with hard particles [13,14]. The strengthening mechanism of these steels leverages solid-state solution hardening of carbon in iron and the substantial dislocation density resulting from the martensitic transformation. Although there are extensive references in the literature discussing the influence of martensite content on the properties of TRIP steels, such as the correlation between martensite fraction and

strength [15–17], martensite fraction and ductility [1,18–20], and the kinetics of deformation and transformation [21,22], among others, the origin of the exceptional ductility in TRIP steels has been a subject of debate. Some authors attributed it to phase transformation strain, but this theory has been mathematically challenged [22,23]. Recent research has experimentally supported the idea that exceptional ductility is closely linked to composite theory, further reinforcing the complexity of these steels [24,25].

In the particular case of TRIP deformation mechanism of AISI 301LN metastable stainless steel, the process begins with the initial annealed state, where the material possesses a stable γ-microstructure [26,27]. As deformation initiates, dislocations are introduced, leading to the formation of stacking faults (SFs) and subsequently triggering the transition from γ-into epsilon (ε-) martensite, characterized by a change in crystal structure. This ε-martensite interacts with the remaining γ-phase, affecting the material's mechanical properties. With continued deformation, particularly under high strain or stress [28–30], nucleation of alpha prime (α'-) martensite occurs at defect sites. The α'-martensite continues to grow within the microstructure, consuming ε-martensite and γ-phases, resulting in the TRIP effect. This growth is accompanied by deformation in the surrounding matrix, contributing to increased ductility and work-hardening behavior, making AISI 301LN stainless steel suitable for applications requiring a combination of strength and ductility (Figure 1).
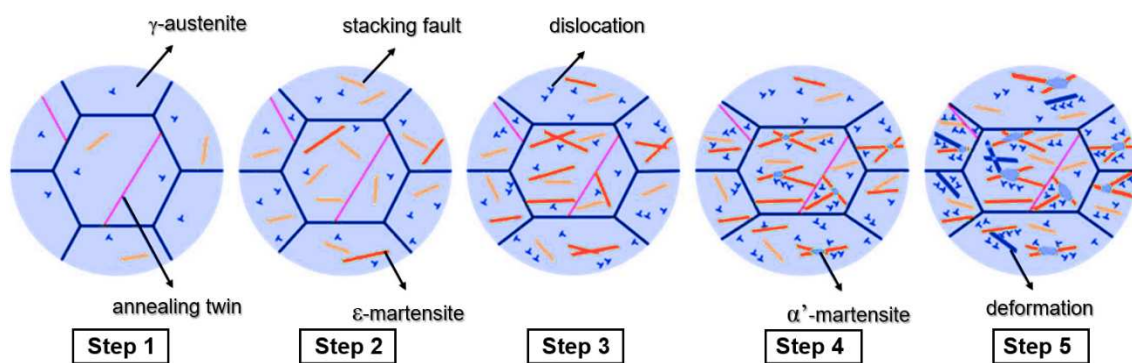

Figure 1. Schematic representation depicting the progression of deformation in AISI 301LN. Adapted from [31].

In this context, it is essential to highlight that the orientation of martensite formation plays a pivotal role in determining the local phase transformation strain. In the subsequent discussion, an analysis of local strain generated during strain-induced martensite transformations and variant selection will be explored [32,33]. Traditionally, the formation of martensite in TRIP materials is mechanically induced, creating intricate microstructures. However, this study departs from tradition by isolating the formation of martensite in a virtually 100% austenitic type AISI 301LN stainless steel. Remarkably, this material undergoes martensitic transformation under room temperature deformation conditions [8,34], providing a unique opportunity for in-depth analysis. Each austenite crystal provides a staggering 24 potential crystallographic variants of martensite that can be induced, resulting in a diverse array of strain and stress distributions within the martensitic plates. This diversity, in turn, influences the material's ability to resist nonuniform deformation and directly impacts its high strength and exceptional ductility.

Laser surface texturing (LST) is an advanced technique that precisely controls the energy of laser beams to create microscale or nanoscale patterns on steel surfaces [35]. This process offers a myriad of advantages, including controlled surface roughness, friction reduction, enhanced wear resistance, and improved corrosion resistance [2]. It does so by manipulating surface microstructures, which can reduce friction, trap lubricants for hydrodynamic lubrication, and extend the service life of steel components. Furthermore, LST allows for customization, enabling engineers to design specific surface textures tailored

to the requirements of diverse applications. This technology not only improves material performance but also reduces environmental impact by decreasing energy consumption and emissions in sectors such as transportation.

The selection of AISI 301LN stainless steel as the focus of this study can be attributed to several compelling reasons. AISI 301LN belongs to the class of metastable austenitic stainless steels, known for their exceptional strength and corrosion resistance. These materials are highly sought after in industries like automotive and aerospace, which demand superior mechanical properties to ensure structural integrity and durability. In particular, AISI 301LN is recognized for its unique combination of strength and ductility, attributed to the presence of strain-induced martensite phase transformations within its austenitic matrix. The austenitic steels offer a promising platform for exploring the effects of LST, which is an emerging and versatile surface modification technique. By studying the influence of LST on AISI 301LN, this research aims to shed light on the potential for further enhancing the mechanical properties of this high-performance steel, thereby addressing the demands of these critical industries more effectively. This manuscript undertakes a comprehensive exploration of the plastic deformation-induced formation of martensite in AISI 301LN stainless steel. It leverages advanced techniques such as electron backscatter diffraction (EBSD) and high-resolution digital image correlation (HRDIC) to provide a detailed view of the material's behavior at various stages of deformation. The primary focus of this investigation centers on strain-induced martensite formation along active {111} slip planes and its interaction with parent austenite slip, with the aim of unravelling microstructural plasticity.

This study is motivated by a comprehensive perspective, as it involves the examination of strain-induced martensite transformations and the relatively unexplored domain of LST. A novel and substantial contribution to the field of materials science is introduced through this multifaceted investigation, which is of direct significance to industries in need of high-performance materials to meet increasing demands. Consequently, the research objectives have been refined to provide improved clarity and insights into the uniqueness of this work. Specifically, these objectives are designed to shed light on the intricate interplay between strain-induced martensite transformations and the impacts of laser surface texturing, thereby presenting new perspectives on microstructural behavior and enhancements in mechanical properties. This effort aims to deliver a more profound understanding of the potential applications of laser surface texturing, particularly concerning the optimization of the mechanical properties of materials such as AISI 301LN stainless steel.

2. Experimental Details

The composition of AISI 301LN metastable austenitic stainless steel used in this study was as follows (wt.%): 17.6% Cr, 6.5% Ni, 1.13% Mn, 0.02% C, 0.17% N, and Fe as the balance. The initial condition of the AISI 301LN was an annealed sheet of 1.5 mm thickness. Grit papers were used to obtain a surface finish with an average roughness of ~0.85 μm. The surface of the samples was then laser-textured with parallel linear patterns aligned with the rolling direction (RD) of the steel sheets. An Explorer-One pulsed laser from Spectra physics (Stahnsdorf, Germany) was used.

The crystal glass of the laser source was Nd: YLF, with a wavelength of 349 nm, a maximum peak power of 60 W, an energy per pulse of 120 μJ, and a beam diameter of 145 μm. In all the tests, the laser parameters used were kept constant and equal to a scanning speed of 6 mm/s, with 68% overlapping of the laser beam spots on the surface; the incident laser beam was maintained at 90 degrees to the target surface, with a frequency of 1 kHz and a laser peak power of 60 W; the pulse duration was 2 μs and, thereby, the energy per pulse was equal to 80 μJ; and the heat input was 6.33 KJ/m. Samples were held on the XYZ-axis stage with a distance between the sample's surface and the nozzle (stand-off distance) of 150 mm and the focal plane located at a distance of 80 mm from the surface (focal length), as shown in Figure 2.
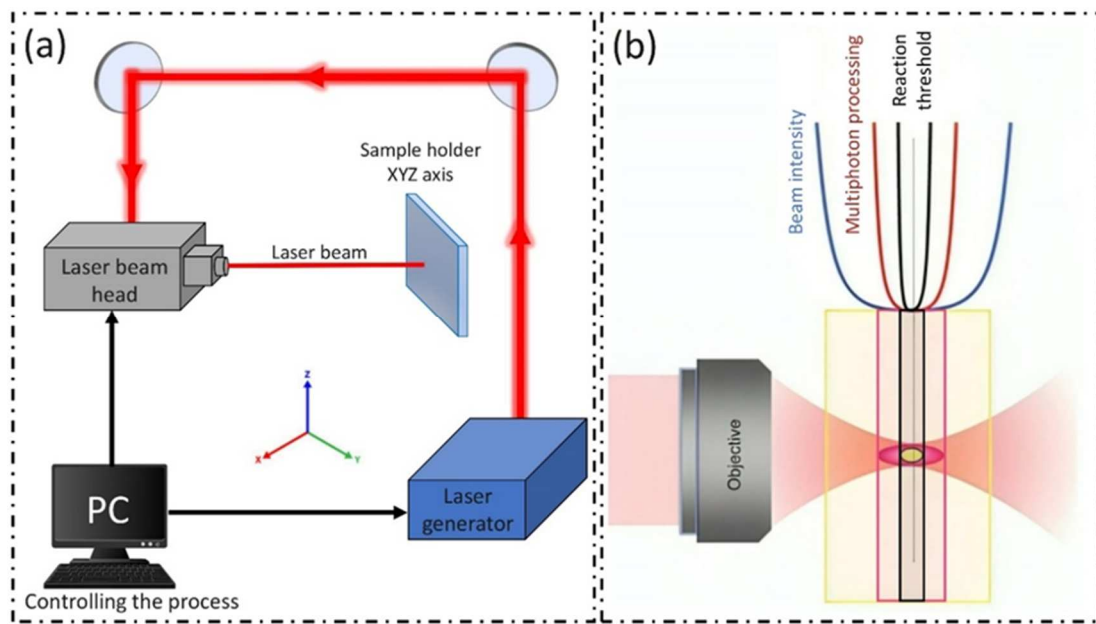
Figure 2. Schematics representation of (**a**) the laser surface texturing process in this study, and (**b**) laser beam focal plan characteristics.

Table 1 gives the tensile properties of AISI 301LN obtained from specimens oriented transversally to the RD.

Table 1. Mechanical properties of AISI 301LN in the as-received state.

Ultimate Tensile Strength (MPa)	Yield Stress (MPa)	Elongation to Fracture (%)	Reduction of Area (%)
734 ± 16	562 ± 11	72 ± 3	77 ± 2

Tensile testing was conducted using six specimens and employing an Instron machine (MA, USA), as illustrated in Figure 3a. Dimensions of the tensile specimens are indicated in Figure 3b. In Figure 3c is a photograph that corresponds to a tensile specimen as it appeared after the laser treatment in its central zone. The tensile rate applied was 10 μm/s.
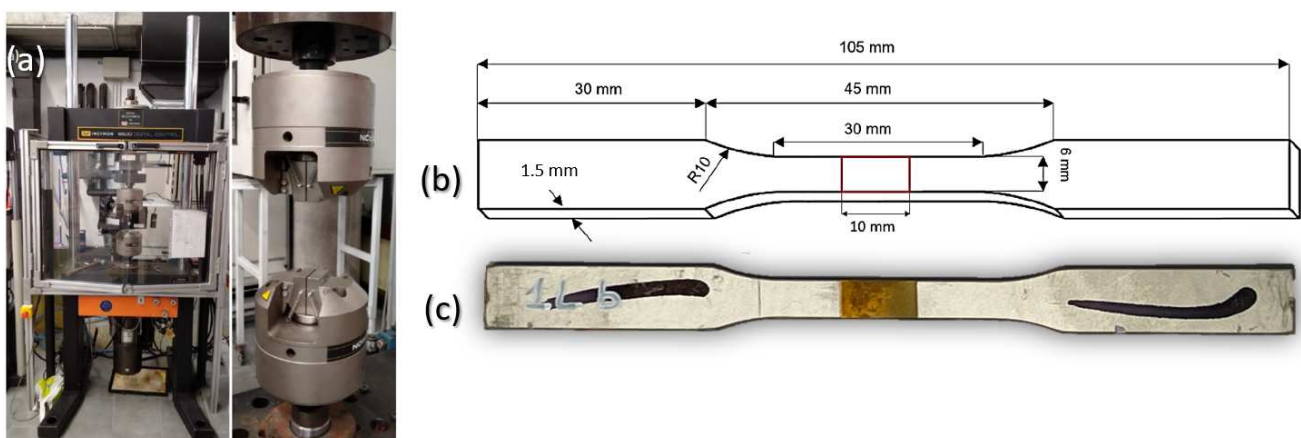

Figure 3. (**a**) Experimental setup of the tensile test machine, (**b**) schematic view and the respective dimensions of the tensile specimen, and (**c**) real photograph of the tensile specimen after LST (the central part corresponds with the textured region by using LST technique).

The analysis of the microstructure and substrates postlaser treatment was conducted utilizing a Neon40 Carl Zeiss SEM (Oberkochen, Germany). Electron backscatter diffraction (EBSD) scans were performed on the external surface, positioned at the center of the tensile specimens, using a Jeol JSM IT800 SEM (Tokyo, Japan) equipped with an EBSD detector. The step size was held constant and equal to 1 μm, and subsequent data analysis was performed using Channel 5 software v3 (Oxford Instruments, Abingdon, UK). XRD measurements were carried out using an Advance D8 X-ray diffractometer equipped with CuKα radiation for phase identification of the laser-treated specimens to determine the quantity of the induced α'-martensite phase during the tensile test.

3. Results and Discussion

3.1. Microstructure

Figure 4 illustrates the XRD patterns of the AISI 301LN stainless steel specimens without and with laser surface texturing. Initially, the microstructure of the initial specimen appeared to be totally γ-phase. However, upon subjecting the material to laser surface texturing, the formation of strain-induced α'-martensite was observed. Although the diffraction peaks of α'-martensite were not easily detectable due to their low intensity, Rezayat et al. [36] reported the presence of a weak α'-martensite peak in the XRD spectrum of AISI 301LN after LST. This α'-martensite phase is characterized by overlapping SFs and a heavily faulted crystal structure, resulting in low-intensity diffraction peaks. Subsequently, as the power of laser surface texturing increased, the intensities of the γ-peaks gradually diminished, while the α'-peaks became more pronounced in the spectra. Eventually, with higher levels of laser surface texturing, the microstructure underwent a significant transformation, primarily consisting of strain-induced α'-martensite due to the intense LST. The changes in XRD intensity observed with laser irradiation can be attributed to the increased presence of the martensitic phase. As more martensite forms within the material due to laser surface texturing, this leads to higher-intensity peaks in the XRD patterns [37].
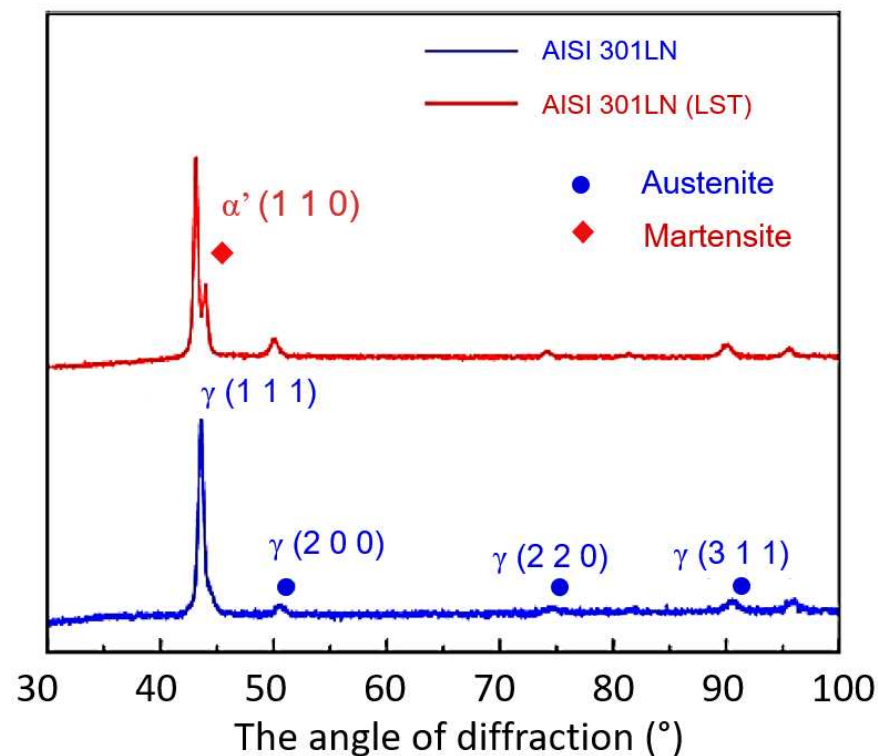

Figure 4. XRD peaks spectra before and after laser surface texturing.

The distinctive peaks of the AISI 301LN specimen after the LST were analyzed employing the Scherrer formula, see Equation (1).

$$D = \frac{Kl}{B\cos\theta} \qquad (1)$$

where D is the mean size of the ordered (crystalline) domains, which may be smaller or equal to the crystalline or particle size, B is the half-height width of the diffraction peak, and K is assigned a value of 0.89. Additionally, θ denotes the Bragg diffraction angle, and l typically denotes the X-ray wavelength, commonly approximated as 1.54 Å. The corresponding parameters are detailed in Table 2, indicating that the LST-induced crystalline size for the α'-phase measured 2.05 Å, whereas the crystalline size for γ-phase on the most prominently diffracted crystal was around 2.09 Å.

Table 2. Crystalline size of AISI 301LN after laser surface texturing.

Parameter	γ (1 1 1)	α (1 1 0)	γ (2 0 0)	γ (2 2 0)	α (2 1 1)	γ (3 1 1)
2θ (°)	43.15	44.02	49.93	74.26	81.39	90.09
B (°)	0.70	0.71	0.82	1.34	1.52	1.78
D (Å)	2.09	2.05	1.82	1.27	1.18	1.08

Metallographic samples were extracted from the clamping end of the tensile specimens and subjected to examination. Both the central and peripheral regions of the metallographic specimen cross-section were meticulously observed using an optical microscope (OM), as illustrated in Figure 5. In Figure 5a, a stable, uniform, single-phase γ-structure can be distinctly discerned. In Figure 5b, specimens also featured a γ-phase, along with α'-martensite; however, there was a marked reduction in the grain size of the γ-grains. Precise measurements of the γ- grain size was performed using a line intercept method, yielding average values of 27.5 and 9 μm before and after LST, respectively.
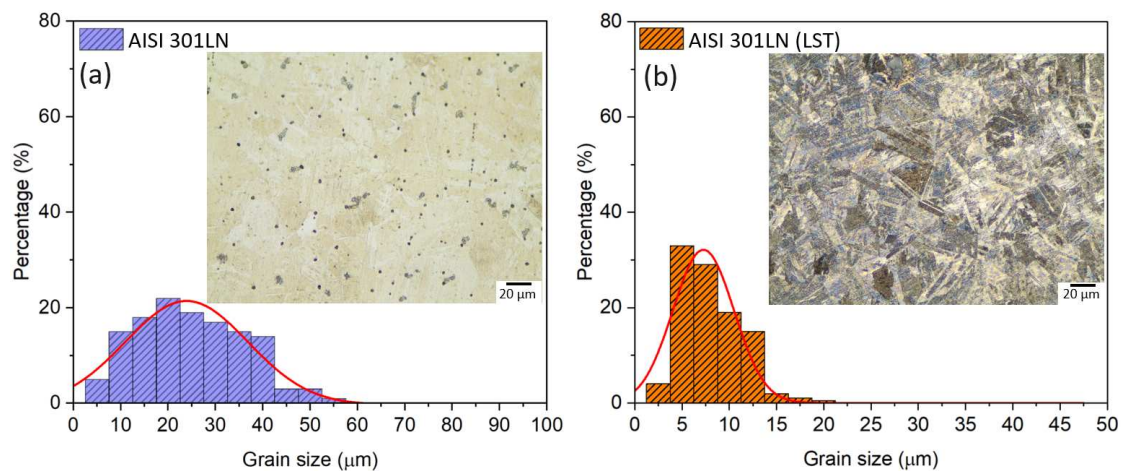

Figure 5. OM and grain-size histogram plots with Gaussian fit of the data: (**a**) before and (**b**) after laser surface texturing.

3.2. Microhardness

Vicker's hardness (HV) tests were conducted on AISI 301LN samples before and after LST, involving three indentations for statistical purposes at the center of each sample in the cross-sectional side. The indentation sizes were carefully measured by means of advanced characterization techniques, and the material's matrix hardness was determined by averaging the measurements from these three points for statistical signification. The obtained matrix HV values before and after LST were 212 HV0.2 and 290 HV0.2, respectively.

The cross-sectional HV variation profiles, depicted in Figure 6, reveal distinct trends: while the HV of AISI 301LN without LST remained consistently within the range of 200 to 212 HV0.2 throughout the cross-section, hardness after LST reached an impressive value of 428.7 HV0.2, more than twice the HV of the underlying steel matrix. Within the first 40 μm from the surface, hardness of AISI 301LN after LST exhibited a sharp decline. However, as the depth increased to the range from 40 to 400 μm, the rate of HV reduction slowed considerably. Beyond a depth of 500 μm, the hardness values displayed minimal variations, stabilizing at approximately 220 HV0.2, a level roughly akin to that of the matrix. The application of LST to the metal surface effectively enhanced the hardness of AISI 301LN. This enhancement was more pronounced within the initial few tens of micrometers, extending up to around six hundred micrometers due to a microstructural change induced during the LST process in agreement with the Hall–Petch equation.
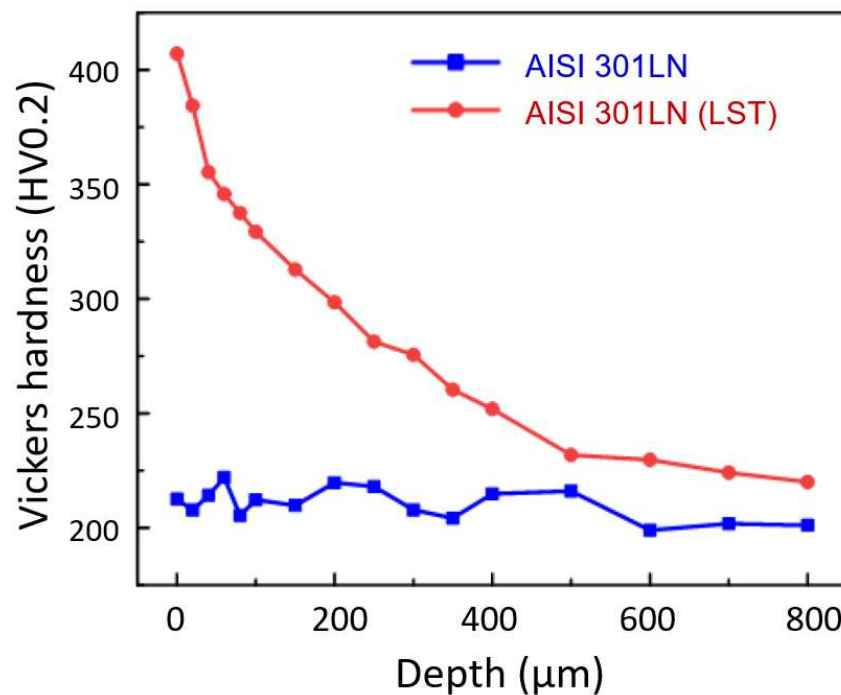

Figure 6. Vicker's hardness evolution as a function of the cross-sectional depth for the nontreated and treated LST specimens.

3.3. Tensile Test Analysis

Figure 7 displays the stress–strain (σ–ε) curves of AISI 301LN specimens before and after LST. Details regarding the tensile properties are summarized in Table 3. Following the LST process, the tensile strength exhibited a notable increase of around 11.85%, while the yield strength surged by 10.85%. In contrast, elongation at fracture and the reduction in the area both saw reductions of 19.44 and 12.98%, respectively.

Table 3. Summary of the main tensile properties of nontreated and LST AISI 301LN.

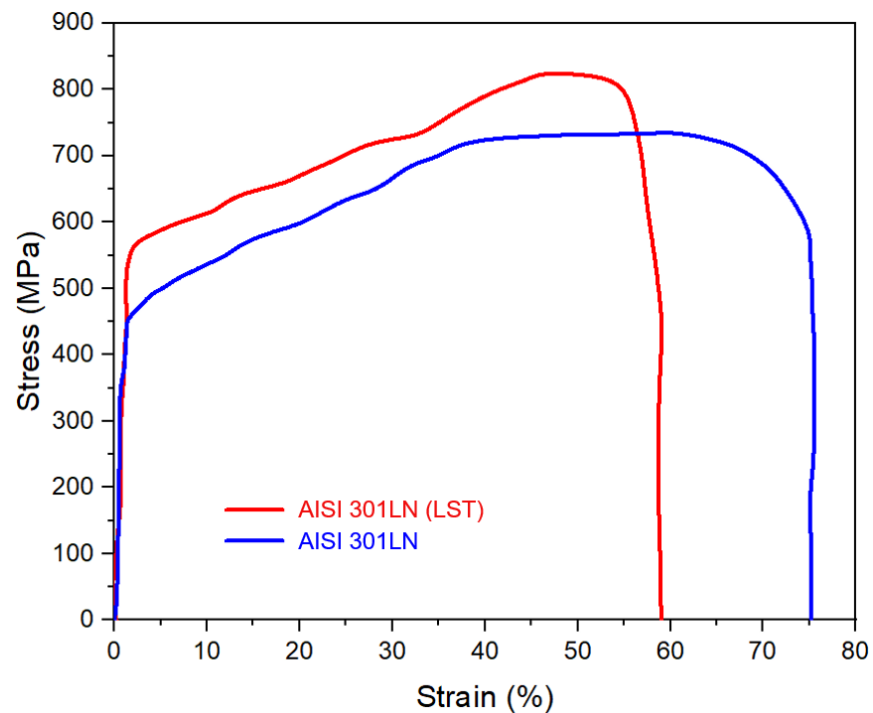| Tensile Properties	301LN	301LN (LST)
Tensile strength (MPa)	734 ± 16	821 ± 12
Yield strength (MPa)	562 ± 11	623 ± 9
Elongation at fracture (%)	72 ± 3	58 ± 2
Reduction in area (%)	77 ± 2	67 ± 3

Figure 7. σ–ε curves for the nontreated (blue) and LST AISI 301LN (red) specimens.

The fracture pattern of AISI 301LN specimens subjected to uniaxial tensile loading is depicted in Figure 8. This fracture pattern featured a bowl-like shape, indicative of a shear fracture that opened at an angle of approximately 45° along the axial direction, accompanied by more pronounced necking. Figure 8b,e illustrate that the stretching stripe distribution on the specimens were uniform. The crack initiation points were identified at the surface, where other material inclusions or grain boundaries were present. Additionally, Figure 8c highlights that the AISI 301LN specimens exhibited a uniform distribution of dimples, representing isometric dimples formed during stretching.
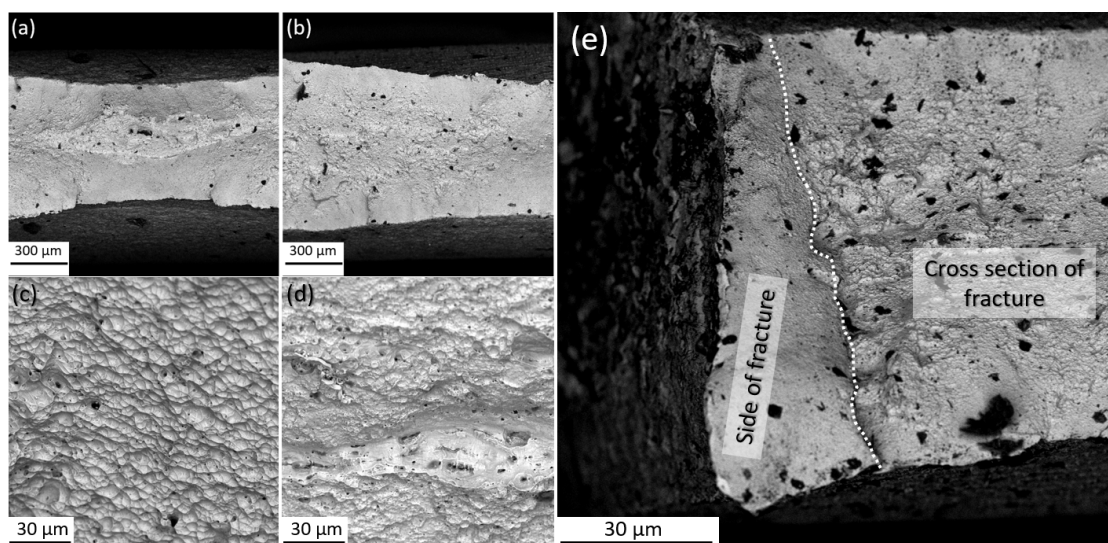

Figure 8. Postmortem micrograph. Morphology of tensile fracture area: (**a**,**b**) general view of as-received and LST AISI 301LN specimens, respectively; (**c**,**d**) central part of the as-received and LST AISI 301LN, respectively; and (**e**) fracture site of LST AISI 301LN.

Figure 8d shows the fracture morphology for the LST AISI 301LN specimens subjected to uniaxial tensile loading. In this instance, the fracture pattern took on an irregular bowl-like shape, as seen in Figure 8b. Although there was not a distinct central rounded bottom, it also indicated a shear fracture that opened at an angle of about 45° along the axial direction. Notably, macroscopic cracks became evident around the bottom region of the specimen's bowl. In contrast to the AISI 301LN specimen, Figure 8b demonstrates that the stretching stripe distribution on the LST AISI 301LN specimen was more disordered and the slip lines were torn. The slip distance remained generally stable, staying within the 10 μm range in depth, which helps explain the limited elongation and reduction in area observed in the LST AISI 301LN specimens. The material edge of the specimen displayed no conspicuous stretching stripes and lacked any additional material inclusions. When considered alongside an overall view of the LST AISI 301LN specimen, it can be concluded that the tensile fracture of the laser-treated specimens originated from the subsurface layer. Subsequently, as the matrix essentially lost its strength, the cracks propagated outward until the LST specimen underwent complete fracture. Lastly, as depicted in Figure 8b,d, the dimples within the treated LST specimen were more uniformly distributed compared to those in the AISI 301LN specimen, although the dimples shared similar sizes.

3.4. Crystallographic Orientation

Figure 9a displays grain orientation (GO) maps for the AISI 301LN metastable austenitic stainless steel specimens at the middle of the sample where it was laser-treated. In the original specimen, the inverse pole figure (IPF) map reveals a distinct and concentrated distribution of dots (see point 1). However, as the AISI 301LN stainless steel underwent tensile deformation, as indicated in points 2 and 3, the orientation within the IPF map became significantly dispersed (Figure 9b). This dispersion signifies lattice rotation resulting from plastic deformation induced during the tensile tests.
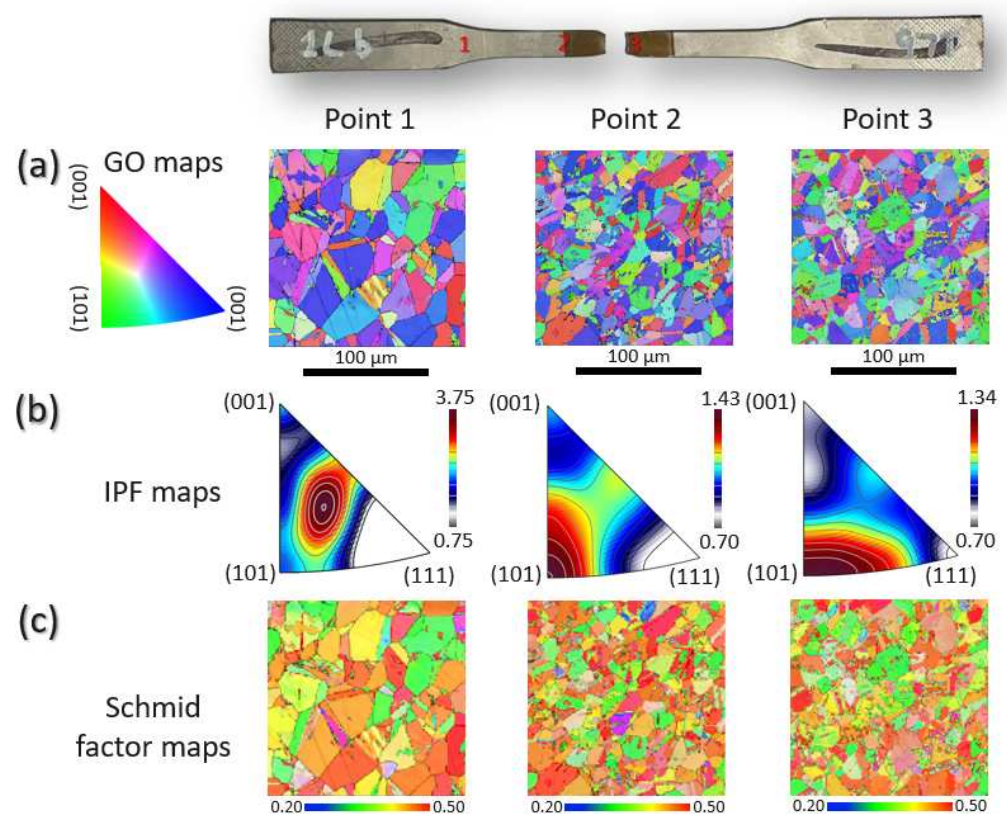

Figure 9. (**a**) Grain orientation maps, (**b**) inverse pole figure maps, and (**c**) the Schmid factor maps of a point labelled in the tensile test specimens.

Previous research [38,39] highlighted that lattice rotation in stainless steel was associated with the activation of slip systems and Schmid factors, further suggesting that softer grains with higher Schmid factor orientations were more prone to slip. In this context, the evolution of the Schimd factors in AISI 301LN stainless steel during tensile tests is depicted in Figure 9c. The Schimd factor calculations were performed using the {111} <110> slip systems of the FCC lattice, and the variation rules were explored through global grain statistics and individual grain analysis.

Figure 10 presents the average Schmid factor values for all pixels within the scanning area. Notably, the average of the Schmid factors reached its peak in the original state (0.43) and exhibited a consistent decrease as plastic deformation progressed, even into the late plastic stage. This reduction in the average of the Schmid factors indicates that lattice slip in the stainless steel becomes increasingly challenging with rising plastic strain.
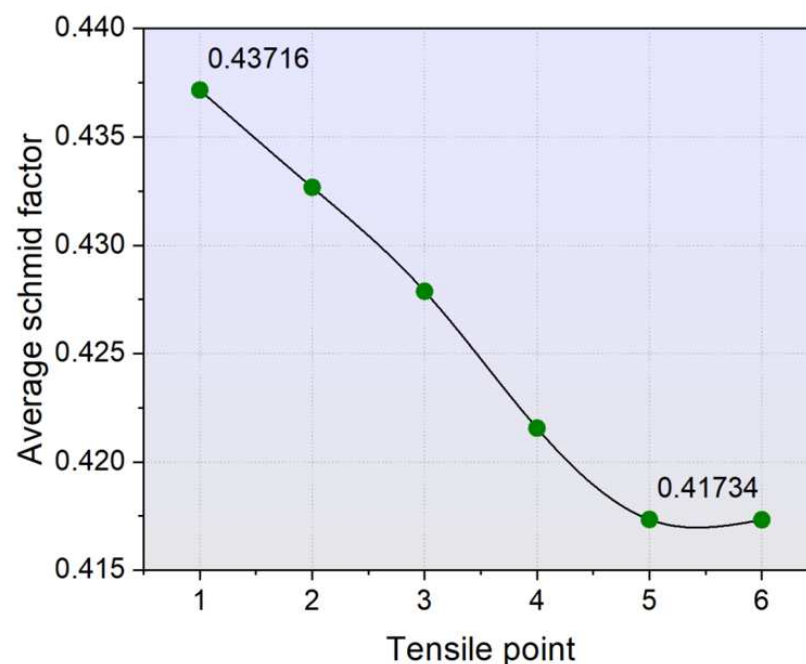

Figure 10. Average value of the Schmid factors for all pixels within the scanning area.

Generally, Schmid factors serve as a parameter for assessing the ease of slip-system activation, with larger Schmid factor values indicating greater susceptibility to movement due to higher shear-stress magnitudes. Further research delves into the internal relationships between lattice orientation, rotation behavior, and Schmid factor variations at the individual grain level.

3.5. Analysis of Grain Characteristics

Figure 11a depicts the GO map and Schmid factor map (Figure 11b) for a defined region within the treated AISI 301LN stainless steel specimen, encompassing grains from a Schmid factor of around 1 to 8. This region holds significance due to the notably high Schmid factor values observed in grains 3 to 5, contrasting with the relatively low values in grains 6 to 8.

Figure 11c provides the average lattice orientation (LO) map for grains 3, 5, 7, and 8, along with their specific Euler angle values. For instance, grain 3 possesses Miller indices of (9, 30, 95) (−6.86, −95.01, 30.43), and its activated slip system is (1−11) [110]. Numerical calculations reveal a φ angle of 46.79° between loading direction X1 and the slip plane normal, and a nearly 43.92° angle λ between X1 and the slip direction, resulting in a high Schmid factor value of 0.492 for grain 3. Similarly, grain 5 exhibits φ and λ angles of 41.17° and 49.24°, respectively, and a Schmid factor value of 0.491. Conversely, grains

7 and 8 display φ and λ angles of 57.71°, 41.95°, and 63.07°, 32.84°, respectively, with corresponding Schmid factor values of 0.397 and 0.378. Notably, the high φ angle in grain 8, despite a small λ angle, yields a low cosine value of 0.4529, significantly diminishing the Schmid factor value.
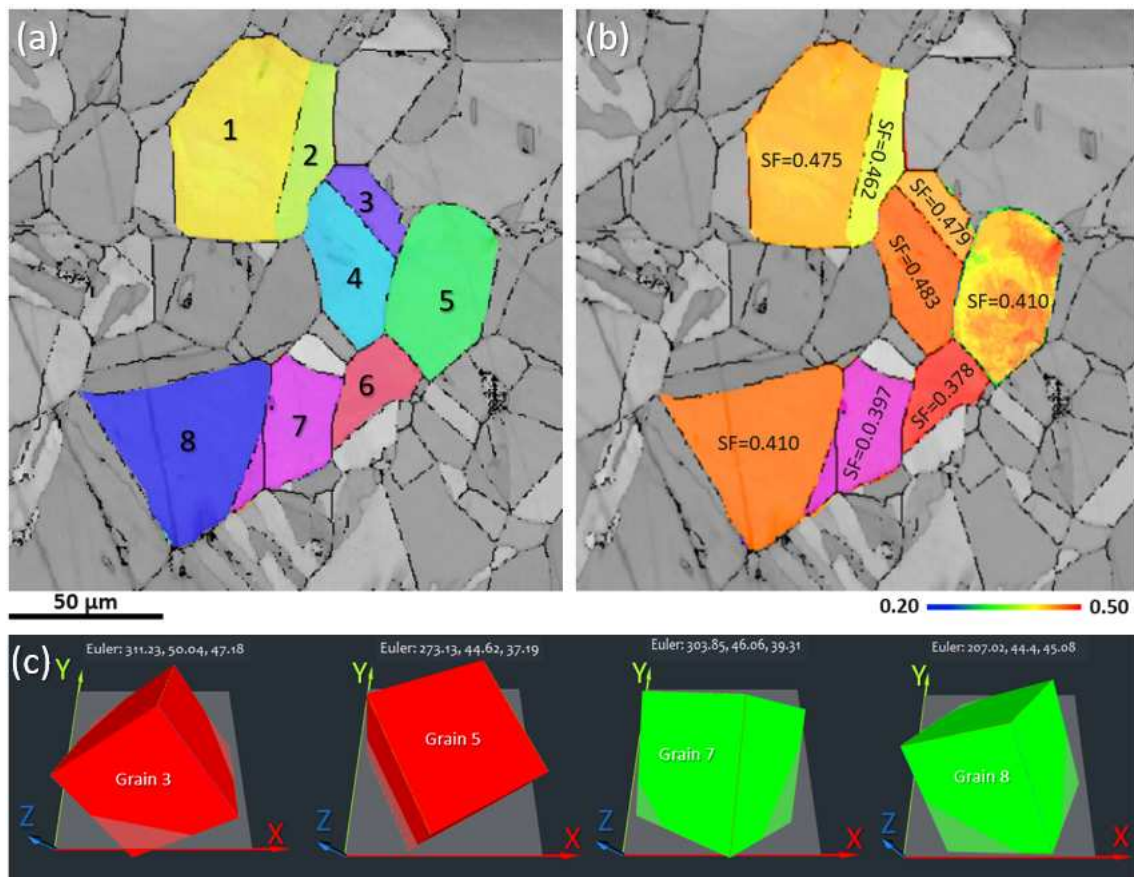

Figure 11. (**a**) SEM micrograph with its corresponding GO map, (**b**) SEM micrograph with its corresponding Schmid factors (SF) map, and (**c**) lattice orientation of grains 3, 5, 7, and 8.

4. Conclusions

In this comprehensive study, an in-depth examination was undertaken to explore the evolution of the Schmid factor within AISI 301LN metastable austenitic stainless steel under tensile testing conditions. A meticulous analysis was conducted, encompassing both grain statistics and individual grain scrutiny, revealing the dynamic relationship between the evolution of the Schmid factor and plastic deformation in the stainless steel. The following key conclusions were drawn from this study:

1. Laser surface texturing (LST) effectively induced the formation of strain-induced α'-martensite in AISI 301LN stainless steel. The initial austenitic microstructure gradually transitioned into a microstructure predominantly comprising α'-martensite with increasing LST power.
2. The α'-phase crystalline size introduced by LST was measured at 2.05 Å, while the γ-grain size on the most strongly diffracted crystal was 2.09 Å, as determined through X-ray diffraction analysis using the Scherrer formula.
3. LST resulted in significant grain refinement, with the average grain size of AISI 301LN stainless steel reduced to 9 μm, which is one-third the size of the as-received grains, as observed through optical microscopy.
4. Remarkable hardness was exhibited by the LST-treated AISI 301LN, reaching 428.7 HV0.2, which was double that of the as-received specimen. This increase in hardness was

most notable within the initial few tens of micrometers, in line with the principles of the Hall–Petch equation.

5. Tensile testing demonstrated that the LST-treated specimens displayed higher ultimate tensile strength and yield strength, with increases of approximately 12% and 11%, respectively, in comparison to the as-received condition. However, it is important to note that reductions of 19% in elongation at fracture and 13% in the reduction in the area were experienced.

References

1. Fargas, G.; Zapata, A.; Roa, J.J.; Sapezanskaia, I.; Mateo, A. Correlation Between Microstructure and Mechanical Properties Before and After Reversion of Metastable Austenitic Stainless Steels. *Metall. Mater. Trans. A* **2015**, *46*, 5697–5707. [CrossRef]
2. Rezayat, M.; Karamimoghadam, M.; Moradi, M.; Casalino, G.; Roa Rovira, J.J.; Mateo, A. Overview of Surface Modification Strategies for Improving the Properties of Metastable Austenitic Stainless Steels. *Metals* **2023**, *13*, 1268. [CrossRef]
3. Dryzek, E.; Sarnek, M.; Wróbel, M. Reverse Transformation of Deformation-Induced Martensite in Austenitic Stainless Steel Studied by Positron Annihilation. *J. Mater. Sci.* **2014**, *49*, 8449–8458. [CrossRef]
4. Ahmmed, K.M.T.; Ling, E.J.Y.; Servio, P.; Kietzig, A.-M. Introducing a New Optimization Tool for Femtosecond Laser-Induced Surface Texturing on Titanium, Stainless Steel, Aluminum and Copper. *Opt. Lasers Eng.* **2015**, *66*, 258–268. [CrossRef]
5. Panov, D.; Pertsev, A.; Smirnov, A.; Khotinov, V.; Simonov, Y. Metastable Austenitic Steel Structure and Mechanical Properties Evolution in the Process of Cold Radial Forging. *Materials* **2019**, *12*, 2058. [CrossRef] [PubMed]
6. Odnobokova, M.; Belyakov, A.; Enikeev, N.; Kaibyshev, R.; Valiev, R.Z. Microstructural Changes and Strengthening of Austenitic Stainless Steels during Rolling at 473 K. *Metals* **2020**, *10*, 1614. [CrossRef]
7. Ke, R.; Hu, C.; Zhong, M.; Wan, X.; Wu, K. Grain Refinement Strengthening Mechanism of an Austenitic Stainless Steel: Critically Analyze the Impacts of Grain Interior and Grain Boundary. *J. Mater. Res. Technol.* **2022**, *17*, 2999–3012. [CrossRef]
8. Mateo, A.; Fargas, G.; Zapata, A. Martensitic Transformation during Fatigue Testing of an AISI 301LN Stainless Steel. *IOP Conf. Ser. Mater. Sci. Eng.* **2012**, *31*, 12010. [CrossRef]
9. Bolgár, M.K.; Nagy, E.; Daróczi, L.; Benke, M.; Mertinger, V.; Beke, D.L. Acoustic Emission During Austenite → ε Martensitic Phase Transformation in TWIP/TRIP Steels. *Metall. Mater. Trans. A* **2019**, *50*, 3495–3501. [CrossRef]
10. Mohamed, H.; Ataiwi, A.; Dawood, J. Mechanical Properties of Martensitic Stainless Steel (AISI420) Subjected to Conventional and Cryogenic Treatments. *Eng. Technol. J.* **2020**, *38*, 1096–1105. [CrossRef]
11. Aprilia, A.; Maharjan, N.; Zhou, W. Decarburization in Laser Surface Hardening of AISI 420 Martensitic Stainless Steel. *Materials* **2023**, *16*, 939. [CrossRef] [PubMed]
12. Zackay, V.F.; Parker, E.R.; Fahr, D.; Bush, R. The Enhancement of Ductility in High-Strength Steels. *Trans. Am. Soc. Met.* **1967**, *60*, 252–259.
13. Saeidi, N.; Raeissi, M.; Vaghei, H.R.; Abdar, M.M. Extraordinary Strength and Ductility Obtained in Transformation-Induced Plasticity Steel by Slightly Modifying Its Chemical Composition. *Mater. Sci. Eng. A* **2017**, *702*, 225–231. [CrossRef]

14. Sohrabi, M.J.; Naghizadeh, M.; Mirzadeh, H. Deformation-Induced Martensite in Austenitic Stainless Steels: A Review. *Arch. Civil. Mech. Eng.* **2020**, *20*, 124. [CrossRef]

15. Tan, X.; He, H.; Lu, W.; Yang, L.; Tang, B.; Yan, J.; Xu, Y.; Wu, D. Effect of Matrix Structures on TRIP Effect and Mechanical Properties of Low-C Low-Si Al-Added Hot-Rolled TRIP Steels. *Mater. Sci. Eng. A* **2020**, *771*, 138629. [CrossRef]

16. Peng, Y.; Huang, H. Mechanical and Magnetic Properties of TRIP690 Steel Strengthened by Strain-Induced Martensite. *J. Magn. Magn. Mater.* **2022**, *550*, 169083. [CrossRef]

17. Alvarez, P.; Muñoz, F.; Celentano, D.; Artigas, A.; Castro Cerda, F.M.; Ponthot, J.-P.; Monsalve, A. Modeling the Mechanical Response of a Dual-Phase Steel Based on Individual-Phase Tensile Properties. *Metals* **2020**, *10*, 1031. [CrossRef]

18. Kelly, P.M. Crystallography of Martensite Transformations in Steels. *Phase Transform. Steels* **2012**, *2*, 3–33. [CrossRef]

19. Panov, D.; Kudryavtsev, E.; Chernichenko, R.; Smirnov, A.; Stepanov, N.; Simonov, Y.; Zherebtsov, S.; Salishchev, G. Mechanisms of the Reverse Martensite-to-Austenite Transformation in a Metastable Austenitic Stainless Steel. *Metals* **2021**, *11*, 599. [CrossRef]

20. Fricke, L.V.; Gerstein, G.; Kotzbauer, A.; Breidenstein, B.; Barton, S.; Maier, H.J. High Strain Rate and Stress-State-Dependent Martensite Transformation in AISI 304 at Low Temperatures. *Metals* **2022**, *12*, 747. [CrossRef]

21. Geijselaers, H.J.M.; Perdahcıoğlu, E.S. Mechanically Induced Martensitic Transformation as a Stress-Driven Process. *Scr. Mater.* **2009**, *60*, 29–31. [CrossRef]

22. Ma, D.; Yang, P.; Gu, X.; Cui, F. Influences of Initial Microstructures on Martensitic Transformation and Textures during Cold Rolling and Tensile Mechanical Properties in High Manganese TRIP Steel. *Mater. Sci. Eng. A* **2022**, *829*, 142147. [CrossRef]

23. Wu, H.; Fan, G. An Overview of Tailoring Strain Delocalization for Strength-Ductility Synergy. *Prog. Mater. Sci.* **2020**, *113*, 100675. [CrossRef]

24. Callens, M.G.; Gorbatikh, L.; Verpoest, I. Ductile Steel Fibre Composites with Brittle and Ductile Matrices. *Compos. Part. A Appl. Sci. Manuf.* **2014**, *61*, 235–244. [CrossRef]

25. Ma, E.; Zhu, T. Towards Strength–Ductility Synergy through the Design of Heterogeneous Nanostructures in Metals. *Mater. Today* **2017**, *20*, 323–331. [CrossRef]

26. Srikanth, S.; Saravanan, P.; Saravanan, D.; Sisodia, S.; Ravi, K.; Bandyopadhyay, A. Improvement in Properties of 301LN Austenitic Stainless Steel for Metro Coach Manufacture. *Adv. Mat. Res.* **2013**, *794*, 201–213. [CrossRef]

27. Pun, L.; Soares, G.C.; Bhusare, S.; Isakov, M.; Hokka, M. Microscale Strain Localizations and Strain-Induced Martensitic Phase Transformation in Austenitic Steel 301LN at Different Strain Rates. *Metals* **2023**, *13*, 207. [CrossRef]

28. Almubarak, A.; Abuhaimed, W.; Almazrouee, A. Corrosion Behavior of the Stressed Sensitized Austenitic Stainless Steels of High Nitrogen Content in Seawater. *Int. J. Electrochem.* **2013**, *2013*, 970835. [CrossRef]

29. Ericsson, T. Residual Stresses Produced by Quenching of Martensitic Steels. *Compr. Mater. Process.* **2014**, *12*, 271–298. [CrossRef]

30. Sun, B.-J.; Xiao, B. Effects of Process Parameters on Interfacial Microstructure, Residual Stresses, and Properties of Tunnel Furnace Brazed Diamonds. *Diam. Relat. Mater.* **2018**, *85*, 98–103. [CrossRef]

31. Ma, Y.; Song, W.; Bleck, W. Investigation of the Microstructure Evolution in a Fe-17Mn-1.5Al-0.3C Steel via In Situ Synchrotron X-Ray Diffraction during a Tensile Test. *Materials* **2017**, *10*, 1129. [CrossRef] [PubMed]

32. Bowles, J.S.; Mackenzie, J.K. The Crystallography of Martensite Transformations I. *Acta Metall.* **1954**, *2*, 129–137. [CrossRef]

33. Celada-Casero, C.; Kooiker, H.; Groen, M.; Post, J.; San-Martin, D. In-Situ Investigation of Strain-Induced Martensitic Transformation Kinetics in an Austenitic Stainless Steel by Inductive Measurements. *Metals* **2017**, *7*, 271. [CrossRef]

34. Luo, C.; Yuan, H. Measurement and Modeling of Deformation-Induced Martensitic Transformation in a Metastable Austenitic Stainless Steel under Cyclic Loadings. *Acta Mater.* **2022**, *238*, 118202. [CrossRef]

35. Rezayat, M.; Moradi, M.; Mateo, A. Nanosecond Pulsed Laser Surface Processing of AISI 301LN Steel: Effect on Surface Topography and Mechanical Properties. *Int. J. Adv. Manuf. Technol.* **2023**, *128*, 3025–3040. [CrossRef]

36. Rezayat, M.; Roa, J.J.; Mateo, A. Phase Transformation and Residual Stresses after Laser Surface Modification of Metastable Austenitic Stainless Steel. In Proceedings of the AIP Conference Proceedings, Malaga, Spain, 5–7 September 2022; p. 020005.

37. Syed, B.; Shariff, S.M.; Padmanabham, G.; Lenka, S.; Bhattacharya, B.; Kundu, S. Influence of Laser Surface Hardened Layer on Mechanical Properties of Re-Engineered Low Carbon Steel Sheet. *Mater. Sci. Eng. A* **2017**, *685*, 168–177. [CrossRef]

38. Mirzadeh, H.; Cabrera, J.M.; Najafizadeh, A.; Calvillo, P.R. EBSD Study of a Hot Deformed Austenitic Stainless Steel. *Mater. Sci. Eng. A* **2012**, *538*, 236–245. [CrossRef]

39. Wang, J.; Huang, M.; Hu, J.; Wang, C.; Xu, W. EBSD Investigation of the Crystallographic Features of Deformation-Induced Martensite in Stainless Steel. *J. Mater. Sci. Technol.* **2021**, *69*, 148–155. [CrossRef]